Surface & Coatings Technology 288 (2016) 105–114

Contents lists available at ScienceDirect

Surface & Coatings Technology

journal homepage: www.elsevier.com/locate/surfcoat

Growth and mechanical properties of epitaxial NbN(001) films on MgO(001)

K. Zhang [a,b], K. Balasubramanian [b], B.D. Ozsdolay [b], C.P. Mulligan [b,c], S.V. Khare [d], W.T. Zheng [a], D. Gall [b,*]

[a] Department of Materials Science, Key Laboratory of Mobile Materials, MOE, and State Key Laboratory of Superhard Materials, Jilin University, Changchun 130012, People's Republic of China
[b] Department of Materials Science and Engineering, Rensselaer Polytechnic Institute, Troy, NY 12180, USA
[c] U.S. Army Armament Research Development and Engineering Center, Benét Laboratories, Watervliet, NY 12189, USA
[d] Department of Physics and Astronomy, University of Toledo, 2801 West Bancroft Street, Toledo, OH 43606, USA

ARTICLE INFO

Article history:
Received 2 December 2015
Revised 6 January 2016
Accepted in revised form 7 January 2016
Available online 11 January 2016

Keywords:
NbN
Reactive sputtering
Epitaxy
Hardness
Elastic constant
Density functional theory
Vacancy

ABSTRACT

NbN_x layers were deposited by reactive magnetron sputtering on MgO(001) substrates in 0.67 Pa pure N_2 at T_s = 600–1000 °C. $T_s \geq 800$ °C leads to epitaxial layers with a cube-on-cube relationship to the substrate: $(001)_{NbN}||(001)_{MgO}$ and $[100]_{NbN}||[100]_{MgO}$. The layers are nearly stoichiometric with $x = 0.95$–0.98 for $T_s \leq 800$ °C, but become nitrogen deficient with $x = 0.81$ and 0.91 for $T_s = 900$ and 1000 °C. X-ray diffraction reciprocal space maps indicate a small in-plane compressive strain of -0.0008 ± 0.0004 for epitaxial layers, and a relaxed lattice constant that decreases from 4.372 Å for $x = 0.81$ to 4.363 Å for $x = 0.98$. This unexpected trend is attributed to increasing Nb and decreasing N vacancy concentrations, as quantified by first-principles calculations of the lattice parameter vs. point defect concentration, and consistent with the relatively small calculated formation energies for N and Nb vacancies of 1.00 and −0.67 eV at 0 K and −0.53 and 0.86 eV at 1073 K, respectively. The N-deficient $NbN_{0.81}(001)$ layer exhibits the highest crystalline quality with in-plane and out-of-plane x-ray coherence lengths of 4.5 and 13.8 nm, attributed to a high Nb-adatom diffusion on an N-deficient growth front. However, it also contains inclusions of hexagonal NbN grains which lead to a relatively high measured hardness $H = 28.0 \pm 5.1$ GPa and elastic modulus $E = 406 \pm 70$ GPa. In contrast, the nearly stoichiometric phase-pure epitaxial cubic $NbN_{0.98}(001)$ layer has a $H = 17.8 \pm 0.7$ GPa and $E = 315 \pm 13$ GPa. The latter value is slightly smaller than 335 and 361 GPa, the isotropic elastic modulus and the [100]-indentation modulus, respectively, predicted for NbN from the calculated $c_{11} = 641$ GPa, $c_{12} = 140$ GPa, and $c_{44} = 78$ GPa. The electrical resistivity ranges from 171 to 437 μΩ cm at room temperature and 155–646 μΩ cm at 77 K, suggesting carrier localization due to disorder from vacancies and crystalline defects.

1. Introduction

Transition metal nitrides have many useful physical properties such as a high hardness, chemical inertness, corrosion resistance, excellent thermal stability and electrical resistivities which vary from metallic to semiconducting [1–7]. As a result, they are widely used as hard wear-resistant coatings, diffusion barriers, and optical thin films [3,4]. Niobium nitride (NbN) has not been studied as extensively as some other transition metal nitrides like TiN. However, it has attracted considerable attention due to its high superconducting transition temperature of 17.3 K [8], and its related potential applications in superconducting electronics including single-photon detectors and tunnel junctions [9,10]. In addition, NbN has potential as a hard protective coating [11,12]. Therefore various researchers have studied the microstructure and mechanical properties of NbN coatings deposited using ion beam assisted deposition [13], pulsed laser deposition [14], cathodic arc deposition [11,12], and reactive magnetron sputtering [15–19]. Deposition using a high ion flux, as obtained by unbalanced magnetron sputtering results in a strong 111 preferred orientation [20], and increasing the nitrogen partial pressure in a Ar/N_2 mixture during deposition leads to an increasing N/Nb ratio in the NbN_x films from $x = 0.61$ to 1.06 and a transition from a pure cubic δ-NbN rocksalt structure to a mixed phase structure including a hexagonal δ′-NbN phase [15]. The reported hardness H of NbN ranges from 7 to 48.5 GPa [11,12,14–18,21]. We attribute this large range to a combination of microstructural effects including open grain boundaries, layer density, texture, and intrinsic stress, but is likely also related to the phases and the N/Nb-ratio, as a transition from the δ to the δ′ phase with an associated increase in x from 0.92 to 1.08 is reported to cause an increase in H from 25 to 40 GPa [15], while an even higher hardness of 48.5 GPa is reported for highly stressed cathodic arc deposited layers [12]. Also, an increase in the nitrogen flow rate or the substrate bias from floating to −200 V yields a transition from cubic-111 to hexagonal-110 preferred orientation, an increase in the biaxial compressive stress from 0.2 to 7.2 GPa, and a transition from δ to δ′, resulting in an increase in H from 14.5 to 37.9 GPa [16,18].

* Corresponding author.
E-mail address: galld@rpi.edu (D. Gall).

http://dx.doi.org/10.1016/j.surfcoat.2016.01.009
0257-8972/

In summary, the different microstructures in reported polycrystalline NbN layers strongly affect the measured mechanical properties. Therefore, it is challenging to determine the intrinsic mechanical properties of NbN from existing studies. An effective approach to deconvolute the intrinsic properties from microstructural effects is to perform property measurements on well characterized single-phase epitaxial layers, as has been previously done for TiN(001) [22], ScN(001) [23], TaN(001) [24,25], HfN(001) [26,27], CrN(001) [28], WN(001) [29], and CeN(001) [30]. Barnett et al. have reported on superlattice hardening in epitaxial Mo/NbN and W/NbN superlattice films [31,32], while the mechanical properties of pure epitaxial NbN(001) layers are not known yet. In contrast, the superconducting properties of epitaxial NbN(001) layers have been studied by various researchers [33–41]. The most common approaches are the growth on MgO(001) substrates by reactive magnetron sputtering [34,38,42] or pulsed laser deposition [43–45]. Extensive work has been done to optimize growth conditions to maximize the critical temperature for superconductivity T_c and achieve a low normal-state resistivity. For example, Wang et al. reported a strong dependence in T_c as a function of the total processing gas pressure and the N_2 partial pressure in an Ar/N_2 gas mixture during sputter deposition at room temperature [42], while Chockalingam et al. studied the effect of sputtering power and N_2 partial pressure during growth at 600 °C [34]. In addition, the lattice parameter of the cubic NbN phase has been found to increase with increasing N_2 partial pressure [34,42,43,46], which can be attributed to a decreasing density of N-vacancies or the possible formation of an ordered phase with both cation and anion vacancies [43,47]. However, details regarding point defects in NbN are still unclear and motivate the first-principles calculations of defect formation energies in our present study. Also, in contrast to the existing investigations on epitaxial NbN(001) that focus primarily on optimizing the superconducting properties, the present work investigates epitaxial NbN(001) as a hard coating material. Correspondingly, opposite to previous studies on NbN(001), growth conditions are chosen in the range commonly used for the epitaxial growth of hard transition metal nitrides, that is, high temperature and pure N_2 gas.

In this paper, we present the results of an investigation on the growth and mechanical properties of epitaxial NbN_x layers deposited on MgO(001) by dc reactive magnetron sputtering in 5 mTorr (0.67 Pa) pure N_2 at substrate temperatures $T_s = 600$–1000 °C. A combination of energy dispersive spectroscopy (EDS) and x-ray diffraction (XRD) shows that layers grown at $T_s = 800$–1000 °C are epitaxial single crystals with an N/Nb ratio $x = 0.81$–0.98 that depends on T_s and causes a decrease in the relaxed lattice constant with increasing x. First-principles calculations of lattice constants vs. point defect density indicate that this decrease can be attributed to increasing Nb and decreasing N vacancy concentrations. Both vacancy types have relatively small formation energies and therefore form due to kinetic constraints during growth. The hardness, elastic modulus, and electrical resistivity are also a function of T_s, due to an increasing crystalline quality with $T_s \leq 900$ °C and a considerable N-vacancy concentration for $T_s \geq 900$ °C.

2. Sample preparation and characterization

The NbN_x films were deposited in a load-locked ultrahigh vacuum DC magnetron sputter deposition system with a base pressure of 10^{-9} Torr (10^{-7} Pa) [48] onto one-side polished $10 \times 10 \times 0.5$ mm^3 MgO(001) wafers that were ultrasonically cleaned in subsequent baths of trichloroethylene, acetone and isopropyl alcohol, rinsed in deionized water, blown dry with dry nitrogen, mounted onto a substrate holder using silver paint, inserted into the deposition system, and degassed for 1 h at 1000 °C using a radiative pyrolytic graphite heater [49]. The heater current was adjusted to reach the desired substrate temperature $T_s = 600$–1000 °C, as measured with a pyrometer that was cross-calibrated by a thermocouple underneath the substrate holder. 99.999% pure N_2 was further purified with a MicroTorr purifier and introduced into the chamber with a needle valve to reach a constant pressure of 0.67 ± 0.01 Pa ($= 5$ mTorr), which was measured with a capacitance manometer and was chosen based on the reported range of 0.4–2.7 Pa for growth of epitaxial transition-metal nitride layers in pure N_2 by reactive sputtering [29,50–61]. A 5-cm diameter 99.95% pure Nb target was positioned 9 cm from a continuously rotating substrate at an angle of 45°, and a constant magnetron power of 300 W was applied, yielding a growth rate of 12 nm/min and a layer thickness after 180 min of deposition of 2.2 ± 0.2 μm, as determined using thickness measurements from scanning electron micrographs of cross-sectional specimens.

The film composition was determined by energy dispersive spectroscopy (EDS) using a FEI Helios Nanolab scanning electron microscope operated with a 0.69–1.4 nA 5.0 keV primary beam and a working distance of 5.0 mm. The spectra were acquired using an Oxford Instruments X-Max^N 80 silicon drift detector which is designed to improve on the typically low light-element sensitivity of EDS quantification. This system has been calibrated using the single beam current Oxford Instruments QCAL approach which takes into account width, position, and shape of each peak profile. The quantitative analysis has been tested with Micro-Analysis Consultants Ltd. produced BN and CaSiO3 standards, indicating an accuracy of the measured N-to-metal ratios of ±2.3%.

X-ray diffraction (XRD) was done using a Panalytical X'pert PRO MPD system with a Cu source and a PIXcel line detector. A divergent beam configuration was used for Ω–2θ scans, while Ω-rocking curves were acquired with an incident parallel beam using an x-ray mirror and limiting the detector receiving angle to 0.27°. XRD ϕ scans were obtained in the parallel-beam mode with Ω and 2θ angles set to detect the NbN 113 reflections at an Ω-offset of 25.153°. Reciprocal space maps around asymmetric 113 reflections were obtained using a hybrid mirror two-bounce monochromator that provides Cu $K\alpha_1$ radiation with a 0.0068° divergence, and a small (~10°) angle between the sample surface and the reflected beam to reduce the beam width which facilitates fast and high-resolution parallel detection over 256 channels in 2θ with the line detector.

Nanoindentation measurements were done using a Hysitron Triboindenter with a maximum load of 10 mN. The area function of the triangular Berkovich diamond tip was calibrated using fused silica, following the procedure described in Ref. [62]. Ten indent sequences were applied for each sample. Each loading-unloading curve was evaluated to detect possible anomalies associated with, for example, particle (dust) surface contamination. As a result, a small fraction (<10%) of outlier curves were excluded from the subsequent data analysis. The resistivity of the coatings was measured using a spring loaded linear four point probe with the sample in air at room temperature (290 K) or immersed in liquid N_2 at 77 K, using a Keithley current source operating at −4.0 to +4.0 mA.

3. Calculations

3.1. Computational approach

First-principles density functional calculations were performed using the Vienna ab initio simulation package (VASP), employing periodic boundary conditions, a plane wave basis set, the Perdew–Burke–Ernzerhof generalized gradient approximation exchange correlation functional [63], and the projector-augmented wave method [64]. All computational parameters are chosen such that calculated total energy differences are converged to within 1 meV/atom. This includes a 500 eV cut-off energy for the plane-wave basis set expansion and a Γ-centered $20 \times 20 \times 20$ k-point grid for an 8-atom conventional unit cell. Nb 4*s*, 4*p*, and 4*d* electrons are explicitly calculated, that is, they are not included in the core of the pseudo potential. Rocksalt niobium nitride NbN_x with $x = 0.75$–1.0 was simulated using a cubic supercell with 32 Nb atoms and 24–32 N atoms that were randomly distributed on anion

sites. Atomic positions were relaxed until an energy convergence of 10^{-4} eV was reached, while keeping the lattice parameter and unit cell shape fixed. Multiple calculations with different lattice parameter are used to determine the relaxed lattice constant and corresponding energy for a given x by fitting the calculated energy vs. lattice parameter (0.1 Å range, 0.01 Å steps) with a second order polynomial.

The formation energy ΔE of various defects, including N and Nb vacancies, anti-site substitutions, and N interstitials were determined using conventional unit cells, and are expressed relative to the zero-temperature energies E_{Nb4N4} and E_{N2} of a defect-free 8-atom conventional NbN unit cell and an N_2 molecule in a 40 × 40 × 40 Å cube for which the N–N distance was relaxed, respectively. That is,

$$\Delta E = E_{\text{defect\_structure}} - n_{Nb}\mu_{Nb} - n_N\mu_N, \quad (1)$$

where $E_{\text{defect\_structure}}$ is the calculated energy of a unit cell containing the defect, n_{Nb} and n_N are the number of Nb and N atoms in this cell, and $\mu_{Nb} = ¼\,(E_{Nb4N4} - 2E_{N2})$ and $\mu_N = ½E_{N2}$ are the chemical potentials of an Nb and an N atom. Every calculated energy corresponds to the minimum of an energy vs. lattice parameter curve, obtained by a parabolic fit through energies calculated for different lattice parameters. These curves provide also values for the relaxed lattice constant of a unit cell containing a defect, which are used in the next section to interpret measured lattice constants. We note here that conventional unit cells containing a single vacancy or an antisite substitution exhibit symmetry which results in no atomic relaxation. In contrast, the unit cell containing an N interstitial requires atomic relaxation, primarily to determine the N–N bond length and orientation on the anion site. Also, all supercell calculations require atomic relaxation.

The three independent elastic constants c_{11}, c_{12} and c_{44} are determined by applying a set of strains to the conventional unit cell, and fitting second order polynomial functions to the calculated elastic energy vs. strain. In particular, c_{11} is determined from tensile and compressive ±1–3% strains along [001], c_{12} is calculated from the bulk modulus B using $c_{12} = (3B - c_{11})/2$ [7] with B being obtained from a fit of the calculated energy vs. lattice constant, and c_{44} is determined using a 1–7% shear strain along [100]. Data fitting using higher (3rd-6th) order functions was employed to estimate the magnitude of non-linear effects, which were found to be small and cause a negligible (1%) uncertainty to the reported elastic constants.

3.2. Computational results

Table 1 is a list of the calculated lattice constants and defect formation energies. The predicted relaxed lattice constant for stoichiometric defect-free rock-salt NbN is 4.419 Å, which is 1.0% larger than the previously reported NbN lattice constant of 4.377 Å (JCPDF 04-004-7058) but agrees well with 4.422 Å from previous predictions using the generalized gradient approximation [65]. The deviation from experiment may be attributed to the generalized gradient approximation, which is known to overestimate lattice constants [66], but may also be related to the presence of both N- and Nb-vacancies, which reduce the measured lattice constant, as discussed below when presenting the experimentally measured values.

A conventional unit cell containing 4 Nb and 3 N atoms is used to simulate an N-vacancy. This calculation, which corresponds to $NbN_{0.75}$ has a lattice constant of 4.379 Å, in good agreement with the previously reported 4.382 Å [65]. The calculated value of 4.379 Å is 0.9% smaller than the calculated value for stoichiometric NbN and suggests, using a linear interpolation, a predicted $a = (4.259 + 0.160x)$ Å as a function of nitrogen content for NbN_x. This is in good agreement with extensive simulations using a 2 × 2 × 2 super cell containing 32 Nb atoms and 24–32 N atoms which are randomly distributed on anion-sites and relaxed to their equilibrium positions. The calculated lattice constants for each composition, corresponding to 24, 25, 26, …, 32 N atoms, indicate a linear composition dependency with $a = (4.259 + 0.159\times)$ Å, in excellent agreement with the prediction from the conventional unit cell. This good agreement suggests that the arrangement of vacancies on the anion sublattice and the corresponding lattice relaxation has only a minor or negligible effect on the predicted lattice constant, and justifies the use of the relatively small conventional unit cell, which is used in the following for all calculations, providing consistency in the approach and limiting computational requirements particularly in the determination of elastic constants.

Correspondingly, the Nb-vacancy was simulated using a cubic unit cell containing 3 Nb and 4 N atoms, yielding a lattice constant of 4.301 Å for $NbN_{1.33}$. Likewise, an Nb or N-antisite substitution where an Nb atom replaces an N atom on an anion site, or vice-versa, results in $a = 4.744$ or 4.368 Å for 8-atom unit cells containing 5 Nb and 3 N atoms corresponding to $NbN_{0.6}$, or 3 Nb and 5 N atoms corresponding to $NbN_{1.67}$, respectively. The N-interstitial is most stable on the tetrahedral site. The corresponding unit cell with 4 Nb and 5 N atoms has a lattice constant of 4.605 Å for $NbN_{1.25}$.

The defect formation energies ΔE listed in Table 1 correspond to the zero-temperature energy difference between the defect configuration and perfect rocksalt NbN, with off-stoichiometry being accounted for by the calculated N_2 molecule energy, as specified in Eq. (1). The formation energies of N and Nb vacancies are relatively small, 1.00 and −0.67 eV, respectively. In contrast, the other defects including Nb and N antisite substitutions and N interstitials have much larger values of 11.95, 5.72, and 2.17 eV. Thus, we expect these latter defects to have negligible concentrations in NbN_x layers deposited in this study and, therefore, do not consider them when discussing the measured lattice constants and elastic constants in the next section of this paper. In fact, we expect negligible Nb antisite substitutions for any realistic experimental conditions while N antisite substitution and/or interstitials may be possible for deposition with highly energetic (>20 eV [23,67]) atomic or molecular nitrogen which impinge on the growth surface and are implanted under conditions where out-diffusion to the growth surface is kinetically inhibited.

The negative value of $\Delta E_{\text{Nb-vacancy}} = -0.67$ eV suggests that the formation of NbN_x with overstoichiometric ($x > 1$) compositions is energetically favored. This negative value is, however, the result from zero-temperature calculations for the defect structure energy as well as the chemical potentials which are both used in Eq. (1). The largest correction at finite temperatures is due to the large entropy of the N_2 gas, which is not considered when determining μ_N, but effectively leads to an increase in $\Delta E_{\text{Nb-vacancy}}$ and a corresponding decrease in $\Delta E_{\text{N-vacancy}}$. In order to estimate these finite temperature effects, we determine in the following a corrected $\mu_N{}^*$ for our experimental conditions of 800 °C and 0.67 Pa: the change in the chemical potential in the vapor phase is due to translational, rotational, and vibrational modes. The characteristic temperatures for N_2 rotational and vibrational modes are 2.86 K and 3340 K [68]. The chemical potential due to the translation, rotational and vibrational modes [68] at 1073 K is −2.84, −0.48 and 0.14 eV, respectively, where the latter value corresponds to the ground-state vibrational energy since the contribution from thermally activated vibrations of −0.004 eV is negligible. In the NbN solid phase, we

Table 1
Calculated lattice constant a of a conventional NbN unit cell containing no crystalline defect, an N or Nb vacancy, an anti-site substitution defect, or a nitrogen interstitial. ΔE indicates the corresponding zero-temperature defect formation energies while ΔE^* is obtained using a corrected chemical potential for equilibrium with a 0.67 Pa N_2 atmosphere at 800 °C.

NbN	a (Å)	ΔE (eV)	ΔE^* (eV)
No defect	4.419	0	0
N-vacancy	4.379	1.00	−0.53
Nb-vacancy	4.301	−0.67	0.86
N-antisite	4.368	5.72	8.78
Nb-antisite	4.744	11.95	8.89
N-interstitial	4.605	2.17	3.70

approximate an N-atom as a single 3D harmonic oscillator, while the rest of the crystal remains fixed. The characteristic vibrational temperature for this oscillator is estimated to be 844 K, based on the calculated $c_{11} = 641$ GPa which yields a spring constant of 284 N/m. This yields a change in chemical potential [68] of −0.06 eV, which is the sum of +0.11 eV from the ground state energy and −0.17 eV from thermally activated vibrations. Thus, we obtain a corrected nitrogen chemical potential $\mu_N{}^* = \mu_N + ½(-2.84 - 0.48 + 0.14)$ eV − (−0.06) eV = μ_N − 1.53 eV. That is, the absolute value of the N chemical potential for our experimental conditions is 1.53 eV larger than the zero-temperature value. We replace μ_N with $\mu_N{}^*$ in Eq. (1) to determine the modified defect formation energies ΔE^* for the approximate experimental conditions, as also listed in Table 1. These values do not include the configurational entropy arising from the spatial arrangement of point defects. Also, they assume thermodynamic equilibrium between the NbN surface and N_2 gas, while all plasma effects including energetic N_2^+-ions and atomic N impinging on the surface as well as temperature gradients within the processing gas are neglected. We also note here that our calculations predict that the stoichiometric hexagonal NbN phase is thermodynamically more stable than rocksalt NbN, with a calculated formation energy for the hexagonal phase that is 0.37 eV per formula unit lower than for the cubic phase. However, our experimental results indicate a clear dominance of the cubic phase, suggesting that kinetic barriers prevent the formation of the hexagonal phase.

The temperature-corrected formation energies ΔE^* listed in Table 1 indicate that both N and Nb vacancies in NbN have relatively low formation energies <1 eV, while antisite substitutions and nitrogen interstitials have ΔE^* values >3 eV and are therefore unlikely, consistent with the zero-temperature results discussed above. However, comparing N and Nb vacancy formation energies, the results are nearly reversed: while zero-temperature leads to a negative $\Delta E_{\text{Nb-vacancy}} = -0.67$ eV and positive $\Delta E_{\text{N-vacancy}} = 1.00$ eV, temperature correction results in a positive $\Delta E^*_{\text{Nb-vacancy}} = 0.86$ eV and a negative $\Delta E^*_{\text{N-vacancy}} = -0.53$ eV. That is, low temperature favors Nb vacancies while equilibrium of NbN with a 0.67 Pa N_2 atmosphere at 800 °C favors N vacancies. The negative vacancy formation energies should in principle lead to large deviations from stoichiometry, which are not observed in our depositions presented below. Therefore, we believe that the conditions of our experiments effectively yield formation energies somewhere between ΔE and ΔE^*, which is attributed to the combined effects of (i) kinetic barriers for N_2 dissociation and/or recombination, (ii) an N_2 atmosphere temperature that is effectively lower than that of the growing NbN layer, and (iii) energetic particles from the plasma including atomic N and N_2^+-ions which impinge on the layer surface and result in collisional dissociation. The presence of atomic N on the growth surface in combination with kinetic barriers that limit thermodynamic equilibration with the N_2 atmosphere effectively increases the nitrogen chemical potential in the gas phase, which, in turn increases $\Delta E^*_{\text{N-vacancy}}$, possibly to positive values. We note that independent of the exact choice of μ_N, the formation energies for both N and Nb vacancies are relatively small and the sum $\Delta E_{\text{Nb-vacancy}} + \Delta E_{\text{N-vacancy}} = 0.33$ eV remains unchanged with changes in μ_N. This value effectively corresponds to the formation energy for a Schottky defect. It is only approximately three times larger than kT, confirming that both Nb and N vacancies need to be considered during growth of NbN. We note here that the NbO structure [69], which can be described as a rock-salt structure with an ordered array of 25% vacancies on both anion and cation sublattices that effectively correspond to a 25% Schottky defect concentration, has been predicted to be less stable than the rock-salt structure for NbN [70], but is, consistent with our above discussion, nearly as stable as the rock-salt structure for various transition metal nitrides [5] and even becomes the equilibrium structure for some nitrides including WN [5,71].

Table 2 lists the calculated elastic constants c_{11}, c_{12} and c_{44} for defect free NbN as well as NbN which contains 25% of N or Nb vacancies. The c_{11}, c_{12} and c_{44} values for defect free NbN are 641, 140, and 78 GPa, respectively. They deviate by up to ~20% from previously reported 701, 115, and 86 GPa [14], which may be attributed to the limited k-point mesh used in this earlier study. The calculated c_{11}, c_{12} and c_{44} correspond to a bulk modulus of $B = 307$ GPa, a Poisson's ratio along the [001] direction of $\nu_{001} = c_{12}/(c_{11} + c_{12}) = 0.18$, a Zener anisotropy ratio $A = 2c_{44}/(c_{11} - c_{12}) = 0.31$, and elastic moduli along [100, 111] directions of $E_{100} = 591$ GPa and $E_{111} = 216$ GPa. These moduli represent the upper and lower bound of the modulus as a function of crystal orientation. One approach to compare the calculated to the experimentally measured elastic modulus, is to assume an isotropic polycrystalline mixture, for which the elastic modulus can be estimated as the Hill's modulus [72], which is obtained from averaging the Voigt and the Reuss approximations, yielding a calculated isotropic modulus for NbN of $E_{\text{isotropic}} = 335$ GPa. However, the nanoindentation measurements in this study are not done on randomly oriented NbN, but on NbN(001) layers. This causes elastic deformation primarily in the 001 direction, but includes also shear and in-plane compression. Vlassak and Nix [73,74] have derived a correction factor which determines the indentation moduli of specific surfaces of single crystals in comparison to their polycrystalline value. Using their reported curves and our calculated anisotropy ratio and isotropic Poisson's ratio $\nu = 0.5 - E/6B$ [75], we determine a correction factor of 1.078, yielding an NbN(001) indentation modulus $M_{001} = 361$ GPa.

The introduction of vacancy defects causes a slight reduction in the bulk modulus, by 7% for N vacancies and 5% for Nb vacancies with a vacancy concentration of 25% each, corresponding to $NbN_{0.75}$ and $NbN_{1.33}$, respectively. In contrast, the corresponding isotropic elastic modulus increases considerably from 335 GPa for defect-free NbN to 399 GPa for $NbN_{0.75}$ containing N vacancies to 457 GPa for $NbN_{1.33}$ containing Nb vacancies. The strong increase in $E_{\text{isotropic}}$ is not due to a pure strengthening of the bonds, since this would also cause an increase in B. Instead, it is attributed to an increase in the bond directionality with the introduction of vacancies. This is evident from the decrease in c_{12} from 140 to 100 GPa, the strong increase in c_{44} from 78 to 137 GPa, and the corresponding decrease in the isotropic ν from 0.31 to 0.23, for NbN to $NbN_{1.33}$, respectively.

We now use the calculated results to predict the lattice parameter and elastic constants of NbN_x as a function of N and Nb vacancy concentrations. Using the calculated lattice constants in Table 1 and assuming a linear composition dependency, the predicted lattice constant for NbN_x is:

$$a = \left(4.419 - 0.160\,C_V^N - 0.475\,C_V^{Nb}\right)\text{Å}, \tag{2}$$

where C_V^N is the concentration of nitrogen vacancies per anion site and C_V^{Nb} is the concentration of Nb vacancies per cation site. Similarly, we determine the indentation modulus as a function of point defect density as:

$$M_{001} = \left(361 + 246C_V^N + 496C_V^{Nb}\right)\text{GPa}. \tag{3}$$

In the following section, Eqs. (2) and (3) are used to interpret the measured lattice constant and elastic modulus, respectively, while the N-to-Nb ratio $x = (-C_V^N)/(1 - C_V^{Nb})$ is measured experimentally.

Table 2
Calculated elastic constants of stoichiometric NbN, $NbN_{0.75}$ containing 25% N-vacancies, and $NbN_{1.33}$ containing 25% Nb-vacancies. $\nu_{\text{isotropic}}$ and $E_{\text{isotropic}}$ are the isotropic Poisson's ratio and elastic modulus, and M_{100} is the predicted elastic modulus that is expected for an indentation experiment on a 001-oriented layer.

	c_{11} (GPa)	c_{12} (GPa)	c_{44} (GPa)	B (GPa)	$\nu_{\text{isotropic}}$	$E_{\text{isotropic}}$ (GPa)	M_{100} (GPa)
NbN	641	140	78	307	0.31	335	361
$NbN_{0.75}$	614	117	116	283	0.26	399	423
$NbN_{1.33}$	672	100	137	291	0.23	457	485

4. Experimental results and discussion

The nitrogen content is a function of the deposition temperature. In particular, the measured N-to-Nb ratio in 2.0-μm-thick NbN_x layers is $x = 0.95$, 0.97, 0.98, 0.81 and 0.91 for $T_s = 600$, 700, 800, 900 and 1000 °C, respectively, with an estimated uncertainty in x of ± 0.02, arising primarily from oxygen and carbon contamination during air exposure prior to compositional analysis, uncertainties due to the difference between the measured spectra and the fitted peak and background, and uncertainties in the instrumental sensitivity factors obtained using calibration with BN and $CaSiO_3$ standards. Based on the EDS results, the NbN_x layers are nearly stoichiometric for $T_s \leq 800$ °C but become nitrogen deficient for $T_s \geq 900$ °C, which is primarily attributed to N vacancies that form during layer deposition by thermally activated recombination and N_2 desorption, as also predicted by our first-principles calculations suggesting a decreasing effective N vacancy formation energy with increasing temperature. This result is also consistent with reports on other transition-metal nitrides which are well known to exhibit relatively large single-phase fields, for example, TiN_x crystallizes in the NaCl-structure for $0.6 < x < 1.2$ [76]. They are also known to become nitrogen deficient if deposited at high temperature including TaN for $T_s \geq 400$ °C [77], HfN for $T_s \geq 650$ °C [27], and CrN for $T_s \geq 730$ °C [28]. We note here that the measured N-to-Nb ratio for the NbN_x layer grown at 900 °C is lower than for $T_s = 1000$ °C. This is opposite to the expected trend and is not well understood, but may be related to minor secondary phase inclusions, as discussed below, or can be explained by two competing thermally activated processes, namely (i) the recombination and desorption (as N_2 molecules) of adsorbed atomic N which stem from the energetic deposition flux including sputtered atomic N and collisionally dissociated N_2^+-ions leading to a reduction in x with increasing $T_s > 800$ °C, and (ii) thermal dissociation of physisorbed N_2 molecules which increase N incorporation for $T_s > 900$ °C. In addition, the temperature dependence of the Nb vacancy concentration, as discussed below, may also affect the kinetics of N incorporation and, in turn, the overall N-to-Nb ratio in the deposited layers.

Fig. 1(a) shows a small section of typical Ω–2θ XRD scans from NbN_x/MgO(001) layers deposited at $T_s = 600$, 700, 800, 900 and 1000 °C. For $T_s \leq 700$ °C, the only feature that is detected over the entire measured 2θ range from 5 to 90° is due to the MgO 002 reflection (not shown), yielding a double peak associated with the Cu $K\alpha_1$ and $K\alpha_2$ lines. This suggests that these NbN_x layers exhibit insufficient long-range crystalline order to be detected by XRD. More specifically, we estimate that the average NbN grain size in these layers is <3 nm, since larger grains, even if randomly oriented, would yield detectable XRD peak(s), based on the peak intensity detection limit for the given measurement setup of 100 cps, and the fact that epitaxial layers with the same thickness presented below exhibit a 10^5 cps peak with a 0.8° rocking curve width and a 10 nm coherence length. That is, $T_s \leq 700$ °C leads to nanocrystalline NbN layers which may be attributed to a δ–δ′ phase instability that leads to a high stacking defect density which causes continuous grain renucleation. In contrast, the NbN_x layer grown at $T_s = 800$ °C shows a well developed XRD peak at 41.331° which is attributed to the 002 reflection for cubic NbN, corresponding to an out-of-plane lattice constant $a_\perp = 4.369$ Å, determined using the weighted average wavelength 1.5418 Å from the Cu $K\alpha_1$ and $K\alpha_2$ lines. Increasing T_s to 900 °C results also in an NbN 002 peak. However, its position is shifted to $2\theta = 41.223°$, its intensity of $I_{200} = 4.4 \times 10^4$ cps is 2.5 times higher than for $T_s = 800$ °C, and the peak shape reveals the doublet of the XRD source, indicating a larger crystalline quality and a higher coherence length, as discussed below. $a_\perp = 4.376$ Å for this layer is determined using the wavelength 1.54056 Å from the Cu $K\alpha_1$ line. In addition, the

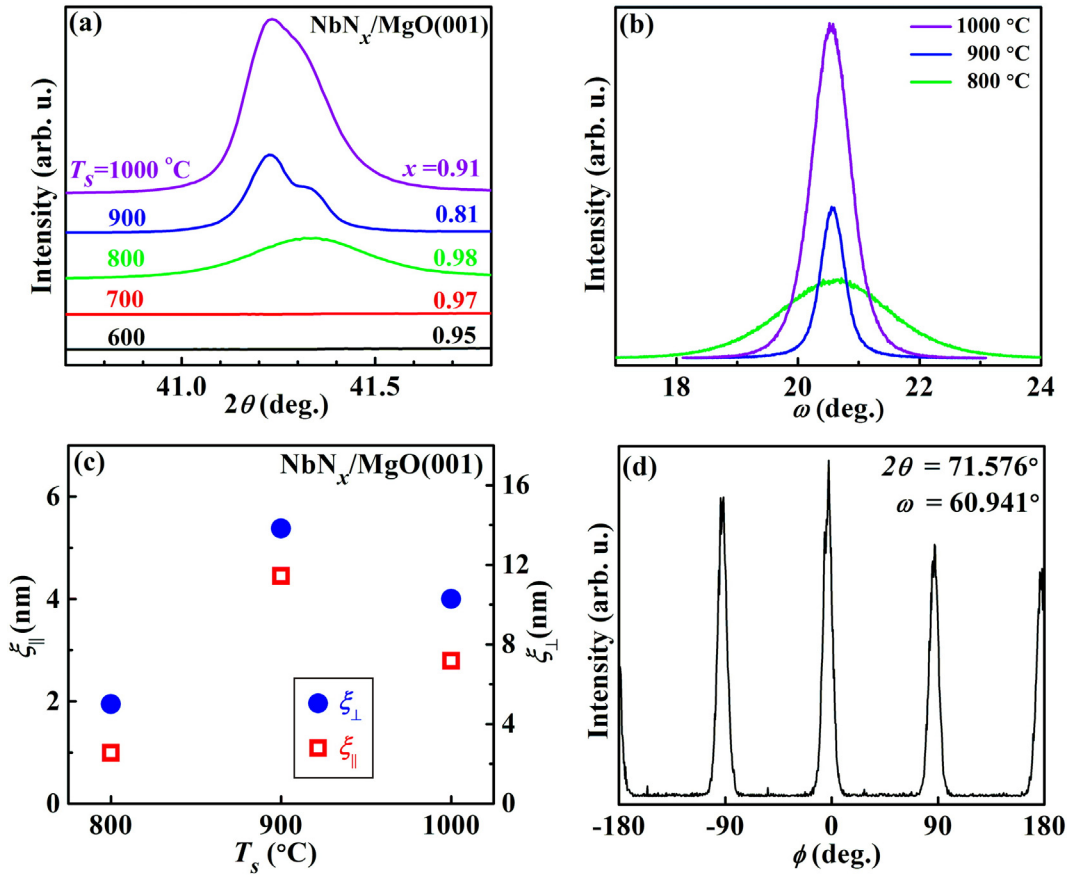

Fig. 1. X-ray diffraction (a) Ω–2θ scans for $T_s = 600$–1000 °C, (b) Ω-rocking curves of the NbN 002 reflection for $T_s = 800$–1000 °C, (c) in-plane $\xi_\parallel$ and perpendicular $\xi_\perp$ x-ray coherence lengths for $T_s = 800$–1000 °C, and (d) ϕ-scan of the NbN 113 reflections for $T_s = 800$ °C, from NbN_x films grown on MgO(001) at temperatures T_s.

$T_s = 900$ °C spectrum also reveals a 100 times weaker (533 counts) peak at $2\theta = 31.732°$ which is close to the reported 31.738° for the 0004 reflection of hexagonal δ′-NbN (JCPDF 20-0801), indicating that this layer contains inclusions of 0001-oriented hexagonal NbN grains. The $T_s = 1000$ °C layer shows no indication of secondary phases but exhibits an intense ($I_{200} = 9.6 \times 10^4$ cps) peak at 41.270° which corresponds to $a_\perp = 4.375$ Å.

Fig. 1(b) shows 002 Ω-rocking curves for NbN films deposited at $T_s = 800$, 900 and 1000 °C, exhibiting full widths at half maximum $\Gamma_\Omega = 2.2°$, 0.49°, and 0.79°, respectively. That is, the $T_s = 900$ °C layer has the narrowest peak, indicating the lowest mosaicity or highest crystalline quality. Somewhat contrary to this trend, the peak intensity increases monotonously with T_s, with the strongest 002 peak for $T_s = 1000$ °C, which can be attributed to the absence of secondary phase inclusions for $T_s = 1000$ °C, and/or temperature induced changes in the N- and Nb-vacancy concentrations and spatial distributions. These results are fully consistent with the Ω–2θ scans in Fig. 1(a), which show the narrowest peak for $T_s = 900$ °C but the highest intensity for $T_s = 1000$ °C. This is illustrated quantitatively in Fig. 1(c), which is a plot of the in-plane and out-of-plane x-ray coherence lengths, $\xi_{||}$ and $\xi_\perp$, which are a measure of the lateral film mosaicity and the mosaicity along the growth direction, respectively. They are obtained from the peak widths Γ_Ω and $\Gamma_{2\theta}$ in Ω-rocking curves and Ω–2θ scans, as described in Ref. [27]. We note that $\Gamma_{2\theta}$ is determined by deconvoluting the peak broadening from the double peak feature associated with the x-ray source doublet. For example, the narrowest peak in Fig. 1(a) from the $T_s = 900$ °C layer has a $\Gamma_{2\theta} = 0.12°$. The in-plane and out-of-plane coherence lengths in Fig. 1(c) show comparable trends, with the highest $\xi_{||} = 4.5$ nm and $\xi_\perp = 13.8$ nm for $T_s = 900$ °C, 38% and 25% lower values for $T_s = 1000$ °C, and the lowest $\xi_{||} = 1.0$ nm and $\xi_\perp = 5.0$ nm for $T_s = 800$ °C. These results confirm that the NbN layer deposited at $T_s = 900$ °C has the highest crystalline quality. We attribute this to the relatively low N-to-Nb ratio of 0.81, as follows: the substoichiometric composition of this layer is due to a relatively low steady-state N coverage of the growing NbN surface, which in turn, facilitates a large cation surface mobility. This argument is based on the related well studied growth of TiN(001), for which the activation energy for cation diffusion in the absence of N is only 0.35 eV [78], but if bonded to an N-adatom increases to 1.1 at low N concentration [79] and 1.4 eV and high N concentration [55], leading to an increase in the Ti adatom mobility and a decrease in the surface roughness from 7.0 to 1.5 Å as x decreases from 1.0 to 0.67 in TiN_x [22].

Fig. 1(d) is an XRD ϕ scan from an NbN layer deposited at 800 °C, which is typical for all layers with $T_s = 800$–1000 °C. It is obtained at fixed $2\theta = 71.576°$ and $\Omega = 60.941°$ to detect NbN 113 reflections, using a constant Ω-offset of 25.153°. During the scan, the sample is rotated about its surface normal by the angle $\phi = -180°$ to 180°. The plot shows four peaks separated by $\Delta\phi = 90°$, indicating an in-plane four-fold rotational symmetry and, together with the results from the Ω–2θ and Ω-rocking curve scans in Fig. 1(a) and (b), establishes that the NbN layers grow epitaxially on MgO(001) with a cube-on-cube orientational relationship with the substrate: $(001)_{NbN} \,||\, (001)_{MgO}$ and $[100]_{NbN} \,||\, [100]_{MgO}$.

Fig. 2 shows the results from XRD reciprocal space maps, which are obtained to determine the strain-state of the NbN_x layers. A typical map around an asymmetric 113 reflection obtained from the layer deposited at $T_s = 900$ °C is shown in Fig. 2(a). Diffracted intensity distributions are plotted as isointensity contours in a logarithmic scale such that the spacing between adjacent contours corresponds to an intensity change by a factor of two. They are shown in reciprocal space where the reciprocal lattice vectors parallel and perpendicular to the surface are determined from the experimental Ω and 2θ using $k_{||} = 2\sin\theta\sin(\Omega - \theta)/\lambda$ and $k_\perp = 2\sin\theta\cos(\Omega - \theta)/\lambda$ [80]. The plot shows a maximum with 1.47×10^5 cps associated with the MgO 113 reflection, and a peak with 3.5×10^3 cps due to the NbN 113 reflection. The in-plane $a_{||}$ and out-of-plane $a_\perp$ lattice parameters are determined from

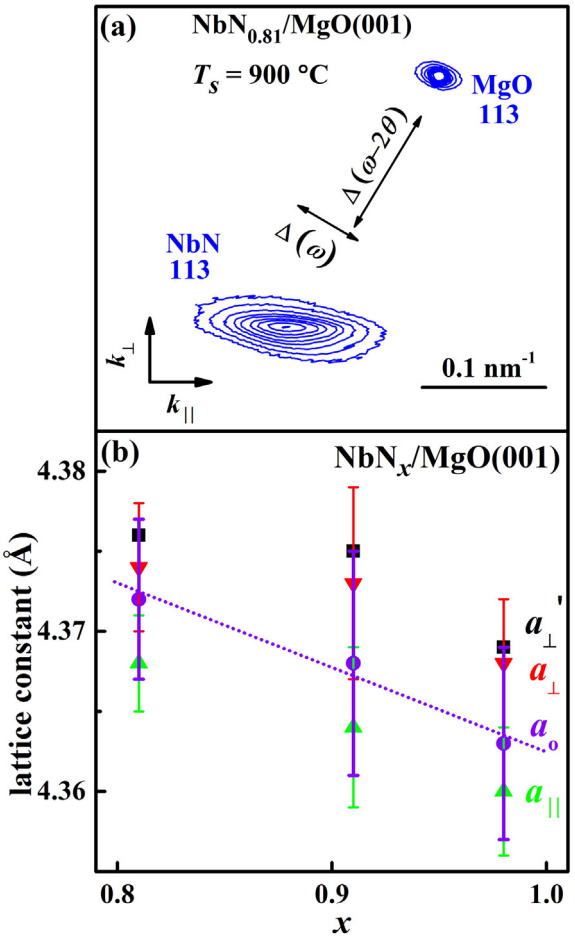

Fig. 2. (a) X-ray diffraction reciprocal lattice map around the 113 reflections of an epitaxial $NbN_{0.81}$ layer grown at $T_s = 900$ °C, and (b) in-plane $a_{||}$, out-of-plane $a_\perp$, and relaxed a_o lattice parameters for epitaxial NbN_x layers as a function of x. The plot also includes the out-of-plane lattice constant $a_\perp'$ obtained from the data in Fig. 1(a), and a linear fit to the a_o values.

this 113 reflection using $a_{||} = \sqrt{2}/k_{||}$ and $a_\perp = 3/k_\perp$, where the MgO 113 peak position within the reciprocal space is fixed to correspond to the relaxed lattice constant $a_{MgO} = 4.212$ Å. This yields $a_{||} = 4.368 \pm 0.003$ Å and $a_\perp = 4.374 \pm 0.004$ Å for this $NbN_{0.81}$ layer deposited at $T_s = 900$ °C. The latter value is in good agreement with $a_\perp = 4.376$ Å from the Ω–2θ scan presented above. We determine the relaxed lattice constant $a_o = 4.372 \pm 0.005$ Å using $a_o = (a_\perp - \nu a_\perp + 2\nu a_{||})/(1 + \nu)$, where $\nu = 0.25 \pm 0.04$ is the Poisson ratio of NbN, as estimated based on reported values of related transition metal nitrides $\nu_{ScN} = 0.20$ [81], $\nu_{TiN} = 0.21$ [82], $\nu_{Hf3N4} = 0.26$ [83] and $\nu_{CrN} = 0.29$ [84]. This value for ν is also consistent with the range of our predicted values for NbN_x which vary with N and Nb vacancy concentration from 0.23–0.31 and 0.13–0.18 for the isotropic and <001> orientation, respectively. As a summary, Fig. 2(b) is a plot of the measured $a_{||}$ and $a_\perp$, and the subsequently determined a_o, as a function of x for NbN_x layers deposited at $T_s \geq 800$ °C. The plot also includes the lattice constants $a_\perp'$, obtained from the Ω–2θ scans presented above, which are in good agreement with the plotted $a_\perp$ values, determined from the reciprocal lattice maps. All layers are in a state of compressive stress, with an in-plane biaxial strain $\varepsilon_{||} = (a_{||} - a_o)/a_o$ of −0.07 to −0.09%, which is nearly independent of x and/or T_s, and is attributed to a combination of differential thermal contraction during cooling from the deposition temperature and the lattice mismatch between the substrate and the layer of 4%.

The relaxed lattice constant decreases from $a_o = 4.372 \pm 0.005$ Å for $NbN_{0.81}$ to $a_o = 4.368 \pm 0.007$ Å for $NbN_{0.91}$ to $a_o = 4.363 \pm 0.006$ Å for

$NbN_{0.98}$, following a nearly linear trend with $da_o/dx = -0.06$ Å, as indicated by the line in Fig. 2(b). Such a negative slope has also been observed by other researchers [85] and indicates that an increasing N-to-Nb ratio causes a decrease in the lattice constant. This trend is opposite to what would be expected if only considering N vacancies to describe the deviation from stoichiometry in NbN_x. In particular, our first-principles calculations on NbN and $NbN_{0.75}$ suggest a positive slope of $da_o/dx = 0.160$ Å for the case when nitrogen vacancies are the only defect affecting the lattice parameter. Similarly, considering bcc Nb metal with an atomic volume of 17.97 $Å^3$, which corresponds to an estimated fcc-Nb lattice constant of 4.158 Å, we predict using a linear interpolation with $a_{NbN} = 4.377$ Å (JCPDF 04-004-7058) a positive $da_o/dx = +0.219$ Å. Therefore, consistent with the relatively low formation energy for both N and Nb vacancies presented in Table 1, we attribute the negative da_o/dx to the presence of both types of vacancies, and use Eq. (2) to interpret the measured a_o vs. x. More specifically, for each sample, we determine the concentration of N and Nb vacancies using Eq. (2) and the measured x and a_o. The nitrogen vacancy concentration decreases with increasing $x = 0.81$, 0.91 and 0.98 from $C_V^N = 21\%$ to 14% and 10%, respectively. Simultaneously the niobium vacancy concentration increases from $C_V^{Nb} = 3\%$ to 6% and 8%. The linear a_o vs. x indicates that N and Nb vacancy concentrations are linearly correlated, with C_V^{Nb} increasing as C_V^N decreases to reach extrapolated values of $C_V^N = C_V^{Nb} = 9\%$ for stoichiometric NbN.

We attribute the correlation of N and Nb vacancy concentrations to growth kinetics. In particular, similar to the case of TiN [22,55,78,79], growth conditions which lead to a supersaturation of N-adatoms result in a high nitrogen incorporation probability, that is a low N-vacancy concentration. However, a high nitrogen surface concentration also results in a relatively low Nb adatom mobility which, in turn, makes it less likely for cation sites to be filled by Nb atoms, resulting in a high Nb vacancy concentration. Conversely, deposition conditions with a limited supply of atomic N on the growth surface result in a higher Nb adatom mobility and a more perfect filling of cation sites, corresponding to a lower Nb vacancy concentration. In addition, a high Nb adatom mobility also leads to a higher crystalline quality, as discussed above.

Fig. 3 is a plot of the measured hardness H and elastic modulus E of NbN_x layers grown on MgO(001) as a function of T_s, as determined from nanoindentation measurements. The hardness plotted in Fig. 3(a) is relatively constant at low growth temperatures, with values of 18.8 ± 1.0, 20.7 ± 2.3, and 17.8 ± 0.7 GPa for T_s = 600, 700, and 800 °C, rises sharply to a maximum H = 28.0 ± 5.1 GPa at T_s = 900 °C, and then drops back to 15.6 ± 1.1 GPa at T_s = 1000 °C. The highest H for T_s = 900 °C may be attributed to the best crystalline quality of this layer. However, the large error bar of this data point, which corresponds to the standard deviation from a total of nine indents, suggests a large non-uniformity for the sample grown at T_s = 900 °C. This is consistent with our XRD analysis which indicates inclusions of a secondary hexagonal NbN phase in this layer. Therefore, we attribute both the high H as well as the large variation to inclusions of hexagonal NbN, which has been reported to exhibit a 60% higher hardness than the cubic phase [15]. The nearly stoichiometric layers (x = 0.95–0.98) deposited at $T_s \le 800$ °C show no evidence for a hexagonal phase. They all exhibit approximately the same hardness of ~19 GPa, which is comparable to the reported hardness of 20.0 ± 0.8 GPa for epitaxial TiN(001) [86] and 21.1 ± 1.1 GPa for ScN(001) [23], but lower than 25.2 ± 0.7 GPa for epitaxial HfN(001) [26], 28.5 ± 1.0 GPa for CrN(001) [28], and 30.8 ± 0.9 GPa for TaN(001) [56]. In contrast, the understoichiometric $NbN_{0.91}$ deposited at 1000 °C also contains no hexagonal NbN but exhibits a lower H = 15.6 ± 1.1 GPa. This decrease in H with increasing N vacancy concentration is opposite to the trend reported for TiN_x, which has been attributed to the vacancy hardening associated with dislocation pinning at point defects [87]. In contrast, the softening with decreasing x in NbN_x may be associated with the increased filling of the 4d bands which reduce the shear modulus and therefore the hardness through enhanced ductility, similar to what

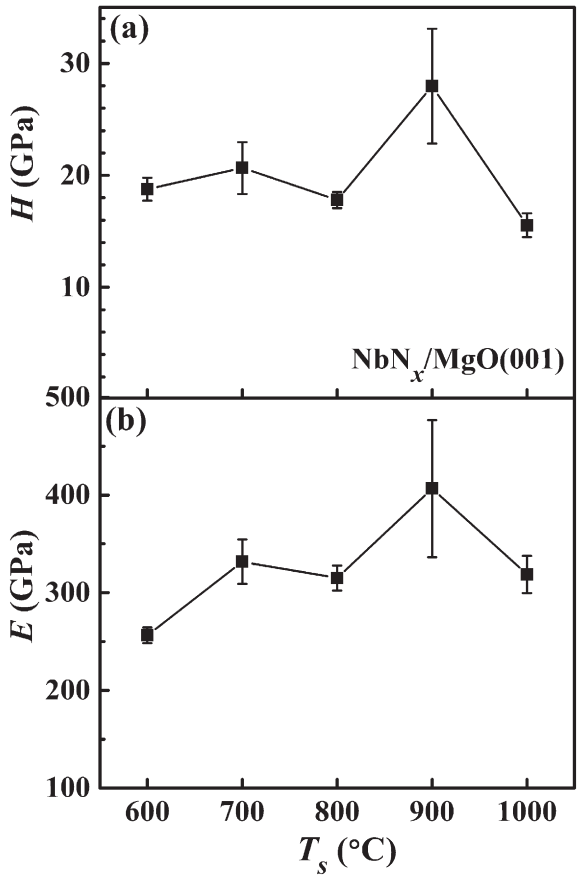

Fig. 3. (a) Hardness H and (b) elastic modulus E, of NbN_x/MgO(001) layers deposited at T_s = 600–1000 °C.

has been reported for the $V_{0.5}Mo_{0.5}N$ system where additional filling of the metal d-bands leads to a reduced shear modulus and an increased ductility [88]. This argument may seem in contradiction with the larger calculated c_{44} for $NbN_{0.75}$ than for NbN presented in Table 2. However, the XRD analysis indicates that the Nb vacancy concentration decreases with increasing N vacancy concentration which may be the primary cause for the softening. This is because the Nb vacancy defect is expected to cause a stronger dislocation pinning effect than an N vacancy, based on the calculated c_{44} value which is even higher for the unit cell containing an Nb vacancy than that containing an N vacancy, as shown in Table 2.

The elastic modulus in Fig. 3(b) shows a similar dependence on T_s as the hardness. It increases from 256 ± 8 GPa for T_s = 600 °C to a maximum E = 407 ± 70 GPa for T_s = 900 °C, and drops back to E = 319 ± 19 GPa for T_s = 1000 °C. The high E value for T_s = 900 °C may be due to the hexagonal inclusions in that sample, while the low E for the polycrystalline layer deposited at T_s = 600 °C may be associated with the low structural order that leads to no detectable XRD peak, suggesting a high degree of bonding disorder which result in a low stiffness. The two phase-pure epitaxial NbN_x layers deposited at T_s = 800 and 1000 °C exhibit nearly the same E = 315 ± 13 and 319 ± 19 GPa, respectively. This seems initially surprising because their N/Nb ratio of x = 0.98 and 0.91 is different, and the predicted indentation modulus M_{100} increases considerably with an increasing N vacancy concentration, as shown in Table 2 for $NbN_{0.75}$. However, M_{100} also increases with an increasing Nb vacancy concentration, and the above XRD analysis together with the predicted lattice constants indicates that an increase in x results in a decrease of both C_V^N and C_V^{Nb}. More specifically, we use Eq. (3) and the values for C_V^N and C_V^{Nb} obtained from the analysis of the measured lattice constants to predict M_{100} = 425 GPa for x = 0.91 and M_{100} = 425 GPa for x = 0.98. That is, we predict the same

indentation modulus for both samples, as the simultaneous decrease in C_V^N and increase in C_V^{Nb} lead to perfect compensation. This is in good agreement with the nanoindentation experiments, which show that these two samples have the same modulus. However, the measured moduli of 315 ± 13 and 319 ± 19 GPa are 25% smaller than the predicted M_{100} = 425 GPa if considering the vacancies, and 6% or 13% smaller than $E_{isotropic}$ = 335 GPa or M_{100} = 361 GPa predicted for stoichiometric NbN. This 6–25% disagreement between experiment and density functional predictions may be attributed to either experimental or theoretical uncertainties. The experimental uncertainties primarily arise from microstructural effects on the nanoindentation measurements, including residual stresses, compositional nonuniformity, surface roughness, layer underdensity, and the inclusion of misoriented grains and/or secondary phase particles. Computational uncertainties arise from the small simulated cell which lead effectively to ordered defect arrays, from nonharmonic elastic constants, from the approximations to determine the indentation modulus from the calculated elastic constants, and from the GGA which is known to overestimate lattice constants and also may cause inaccuracies in the elastic constants of 10–20% [66].

Fig. 4 shows the resistivity ρ of NbN_x layers as a function of their growth temperature, measured both at room temperature (290 K) and 77 K. The room temperature resistivity decreases continuously from ρ_{290K} = 473 μΩ cm for T_s = 600 °C to a minimum ρ_{290K} = 171 μΩ cm for T_s = 900 °C, and then increases again to ρ_{290K} = 401 μΩ cm for T_s = 1000 °C. The data for 77 K shows a similar trend, decreasing from ρ_{77K} = 646 to 155 μΩ cm for T_s = 600–900 °C, and increasing to ρ_{77K} = 637 μΩ cm for T_s = 1000 °C. The resistivity at low temperature is higher for all but the T_s = 900 °C layer, indicating that carrier localization effects dominate electron transport. A similar negative temperature coefficient of resistivity (TCR) has been reported for other epitaxial transition metal nitride layers and has been attributed to a weak Anderson localization due to (i) N-vacancies for CrN(001) [89,90], WN(111) [29], and HfN_x(001) [27]; (ii) anti-site substitutions for TaN_x(001) [24]; (iii) random cation solid solutions for $Sc_{1-x}Ti_xN$(001) [91], $Ti_{1-x}W_xN$(001) [52], and $Sc_{1-x}Al_xN$(001) [92]; and (iv) random cation solid solutions for NbC_xN_{1-x}(001) [93]. Consistent with this observation, we attribute the changes in ρ with deposition temperature of NbN_x/MgO(001) layers primarily to carrier localization effects, which themselves are controlled by the crystalline quality and the vacancy concentrations. More specifically, the resistivity decreases with increasing T_s < 900 °C and increases for T_s > 900 °C. This trend perfectly matches the trend in crystalline quality observed by XRD, which show the highest crystalline quality for T_s = 900 °C, corresponding to the lowest defect-induced carrier localization and therefore the lowest resistivity. In fact, $\rho_{77K} < \rho_{290K}$ for T_s = 900 °C, which corresponds to a metallic TCR and suggests either (i) competing effects of carrier localization and resistivity due to phonon-scattering, with the second effect dominating, or (ii) conventional metallic conduction with, however, defect scattering dominating over phonon scattering since ρ_{77K} is only 9.6% lower than ρ_{290K}. In addition, carrier localization is also affected by the vacancy concentrations. In particular, ρ for T_s = 1000 °C is larger than for T_s = 800 °C, although its crystalline quality is higher. This is attributed to localization due to vacancies. In particular, C_V^N = 10% and C_V^{Nb} = 8% for T_s = 800 °C and C_V^N = 14% and C_V^{Nb} = 6% for T_s = 1000 °C, indicating that both vacancy concentrations change with T_s and the total point defect concentration is slightly larger for T_s = 1000 °C than T_s = 800 °C.

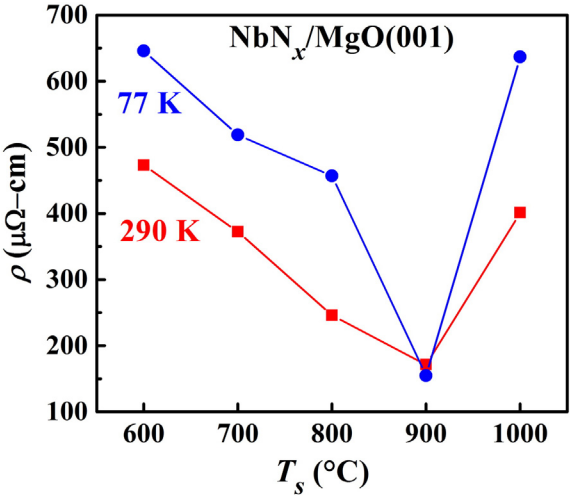

Fig. 4. Resistivity ρ measured at room temperature (290 K) and 77 K, of NbN_x layers deposited at T_s = 600–1000 °C.

5. Conclusions

Density functional calculations using the generalized gradient approximation indicate that the formation energy of nitrogen and niobium vacancies in NbN are relatively small, 1.00 and −0.67 eV at zero temperature and −0.53 eV and 0.86 eV at experimental temperatures, respectively. In contrast, anti-site substitutions and interstitials have considerably higher formation energies and are unlikely to form during NbN thin film deposition. The predicted elastic constants of NbN are c_{11} = 641 GPa, c_{12} = 140 GPa, and c_{44} = 78 GPa. Introduction of N or Nb vacancies leads a slight reduction in the bulk modulus but a considerable increase in the elastic modulus.

NbN_x layers deposited by reactive magnetron sputtering on MgO(001) substrates in 5 mTorr pure N_2 at $T_s \geq$ 800 °C are epitaxial layers with a cube-on-cube relationship to the substrate: $(001)_{NbN}||(001)_{MgO}$ and $[100]_{NbN}||[100]_{MgO}$, but the layer grown at T_s = 900 °C also contains small inclusions of hexagonal-phase grains. X-ray diffraction analyses indicate a small in-plane compressive strain of −0.0008 ± 0.0004 for all epitaxial samples, and a relaxed lattice constant that decreases approximately linearly from 4.372 Å for x = 0.81 to 4.363 Å for x = 0.98. This decrease indicates, in combination with calculated lattice constants for pure and point-defect containing NbN, that the NbN layers contain N and Nb vacancies with decreasing and increasing densities, respectively, from C_V^N = 21% and C_V^{Nb} = 3% for x = 0.81, to C_V^N = 10% and C_V^{Nb} = 8% for x = 0.98. The $NbN_{0.98}$(001) layer deposited at T_s = 800 °C has a hardness H = 17.8 ± 0.7 GPa. T_s = 900 °C leads to the highest crystalline quality with in-plane and out-of-plane x-ray coherence lengths of 4.5 and 13.8, but also the formation of hexagonal grains within the epitaxial cubic matrix, leading to an increased H = 28.0 ± 5.1 GPa. The high crystalline quality of this layer is attributed to the limited nitrogen on the growing NbN(001) surface, which leads to a relatively high Nb adatom diffusion but also a large nitrogen vacancy concentration of 21%. The measured elastic moduli for the epitaxial phase-pure layers deposited at 800 and 1000 °C are 315 ± 13 and 319 ± 19 GPa, respectively. These values are slightly smaller than the first-principles predictions for the stoichiometric NbN isotropic elastic modulus $E_{isotropic}$ = 335 GPa and indentation modulus M_{100} = 361 GPa. Considering the expected N and Nb vacancies yield a larger predicted M_{100} = 425 GPa. The electrical resistivity is dominated by carrier localization and strongly depends on T_s. It ranges from 171 to 437 μΩ cm at room temperature and from 155 to 646 μΩ cm at 77 K.

Acknowledgements

The authors acknowledge support by the National Science Foundation under Grant Nos. 1309490, 1537984, 1234777, and 1234872, and computational resources from the Computational Center for Nanotechnology Innovations at RPI. Kan Zhang thanks the Chinese Scholarship Council for financial support.

References

[1] L. Hultman, Thermal stability of nitride thin films, Vacuum 57 (2000) 1–30.

[2] B.O. Johansson, J.E. Sundgren, J.E. Greene, A. Rockett, S.A. Barnett, Growth and properties of single crystal TiN films deposited by reactive magnetron sputtering, J. Vac. Sci. Technol. A 3 (1985) 303–307.
[3] D. Papaconstantopoulos, W. Pickett, B. Klein, L. Boyer, Electronic properties of transition-metal nitrides: the group-V and group-VI nitrides VN, NbN, TaN, CrN, MoN, and WN, Phys. Rev. B 31 (1985) 752–761.
[4] J. Musil, Hard and superhard nanocomposite coatings, Surf. Coat. Technol. 125 (2000) 322–330.
[5] Z.T.Y. Liu, X. Zhou, D. Gall, S.V. Khare, First-principles investigation of the structural, mechanical and electronic properties of the NbO-structured 3d, 4d and 5d transition metal nitrides, Comput. Mater. Sci. 84 (2014) 365–373.
[6] Z.T.Y. Liu, X. Zhou, S.V. Khare, D. Gall, Structural, mechanical and electronic properties of 3d transition metal nitrides in cubic zincblende, rocksalt and cesium chloride structures: a first-principles investigation, J. Phys. Condens. Matter 26 (2014) 025404.
[7] Z.T.Y. Liu, D. Gall, S.V. Khare, Electronic and bonding analysis of hardness in pyrite-type transition-metal pernitrides, Phys. Rev. B 90 (2014) 134102.
[8] K.S. Keskar, T. Yamashita, Y. Onodera, Superconducting transition temperatures of R. F. sputtered NbN films, Japan, J. Appl. Phys. 10 (1971) 370–374.
[9] G.N. Goltsman, O. Okunev, G. Chulkova, A. Lipatov, A. Semenov, K. Smirnov, B. Voronov, A. Dzardanov, C. Williams, R. Sobolewski, Picosecond superconducting single-photon optical detector, Appl. Phys. Lett. 79 (2001) 705.
[10] Z. Wang, H. Terai, A. Kawakami, Y. Uzawa, Interface and tunneling barrier heights of NbN/AlN/NbN tunnel junctions, Appl. Phys. Lett. 75 (1999) 701.
[11] N. Cansever, M. Danışman, K. Kazmanlı, The effect of nitrogen pressure on cathodic arc deposited NbN thin films, Surf. Coat. Technol. 202 (2008) 5919–5923.
[12] A. Bendavid, P.J. Martin, T.J. Kinder, E.W. Preston, The deposition of NbN and NbC thin films by filtered vacuum cathodic arc deposition, Surf. Coat. Technol. 163-164 (2003) 347–352.
[13] Y. Gotoh, M. Nagao, T. Ura, H. Tsuji, J. Ishikawa, Ion beam assisted deposition of niobium nitride thin films for vacuum microelectronics devices, Nucl. Inst. Methods Phys. Res. B 148 (1999) 925–929.
[14] M.A. Mamun, A.H. Farha, A.O. Er, Y. Ufuktepe, D. Gu, H.E. Elsayed-Ali, A.A. Elmustafa, Nanomechanical properties of NbN films prepared by pulsed laser deposition using nanoindendation, Appl. Surf. Sci. 258 (2012) 4308–4313.
[15] M. Benkahoul, E. Martinez, A. Karimi, R. Sanjinés, F. Lévy, Structural and mechanical properties of sputtered cubic and hexagonal NbNx thin films, Surf. Coat. Technol. 180-181 (2004) 178–183.
[16] M. Wen, C.Q. Hu, Q.N. Meng, Z.D. Zhao, T. An, Y.D. Su, W.X. Yu, W.T. Zheng, Effects of nitrogen flow rate on the preferred orientation and phase transition for niobium nitride films grown by direct current reactive magnetron sputtering, J. Phys. D. Appl. Phys. 42 (2009) 035304.
[17] Z.H. Han, X.P. Hu, J.W. Tian, G.Y. Li, M.Y. Gu, Magnetron sputtered NbN thin films and mechanical properties, Surf. Coat. Technol. 179 (2004) 188–192.
[18] M. Wen, C.Q. Hu, C. Wang, T. An, Y.D. Su, Q.N. Meng, W.T. Zheng, Effects of substrate bias on the preferred orientation, phase transition and mechanical properties for NbN films grown by direct current reactive magnetron sputtering, J. Appl. Phys. 104 (2008) 023527.
[19] V.I. Ivashchenko, P.L. Skrynskii, O.S. Litvin, A.D. Pogrebnjak, V.N. Rogoz, G. Abadias, O.V. Sobol', A.P. Kuz'menko, Structure and properties of nanostructured NbN and Nb-Si-N films depending on the conditions of deposition: experiment and theory, Phys. Met. Metallogr. 116 (2015) 1015–1028.
[20] J.J. Olaya, S.E. Rodil, S. Muhl, Comparative study of niobium nitride coatings deposited by unbalanced and balanced magnetron sputtering, Thin Solid Films 516 (2008) 8319–8326.
[21] H. Ju, J. Xu, Microstructure and tribological properties of NbN-Ag composite films by reactive magnetron sputtering, Appl. Surf. Sci. 355 (2015) 878–883.
[22] C.S. Shin, S. Rudenja, D. Gall, N. Hellgren, T.Y. Lee, I. Petrov, J.E. Greene, Growth, surface morphology, and electrical resistivity of fully strained substoichiometric epitaxial TiNx ($0.67 <= x < 1.0$) layers on MgO(001), J. Appl. Phys. 95 (2004) 356–362.
[23] D. Gall, I. Petrov, N. Hellgren, L. Hultman, J.E. Sundgren, J.E. Greene, Growth of poly- and single-crystal ScN on MgO (001): role of low-energy N-2(+) irradiation in determining texture, microstructure evolution, and mechanical properties, J. Appl. Phys. 84 (1998) 6034–6041.
[24] C.S. Shin, D. Gall, Y.W. Kim, P. Desjardins, I. Petrov, J.E. Greene, M. Oden, L. Hultman, Epitaxial NaCl structure delta-TaNx(001): electronic transport properties, elastic modulus, and hardness versus N/Ta ratio, J. Appl. Phys. 90 (2001) 2879–2885.
[25] C.S. Shin, Y.W. Kim, N. Hellgren, D. Gall, I. Petrov, J.E. Greene, Epitaxial growth of metastable delta-TaN layers on MgO(001) using low-energy, high-flux ion irradiation during ultrahigh vacuum reactive magnetron sputtering, J. Vac. Sci. Technol. A 20 (2002) 2007–2017.
[26] H.S. Seo, T.Y. Lee, J.G. Wen, I. Petrov, J.E. Greene, D. Gall, Growth and physical properties of epitaxial HfN layers on MgO(001), J. Appl. Phys. 96 (2004) 878–884.
[27] H.S. Seo, T.Y. Lee, I. Petrov, J.E. Greene, D. Gall, Epitaxial and polycrystalline HfNx ($0.8 <= = x <= = 1.5$) layers on MgO(001): film growth and physical properties, J. Appl. Phys. 97 (2005) 083521.
[28] D. Gall, C.S. Shin, T. Spila, M. Oden, M.J.H. Senna, J.E. Greene, I. Petrov, Growth of single-crystal CrN on MgO(001): effects of low-energy ion-irradiation on surface morphological evolution and physical properties, J. Appl. Phys. 91 (2002) 3589–3597.
[29] B.D. Ozsdolay, C.P. Mulligan, M. Guerette, L. Huang, D. Gall, Epitaxial growth and properties of cubic WN on MgO(001), MgO(111), and Al2O3(0001), Thin Solid Films 590 (2015) 276–283.
[30] T.Y. Lee, D. Gall, C.S. Shin, N. Hellgren, I. Petrov, J.E. Greene, Growth and physical properties of epitaxial CeN layers on MgO(001), J. Appl. Phys. 94 (2003) 921–927.
[31] A. Madan, X. Chu, S.A. Barnett, Growth and characterization of epitaxial Mo/NbN superlattices, Appl. Phys. Lett. 68 (1996) 2198.
[32] A. Madan, Y.Y. Wang, S.A. Barnett, C. Engstrom, H. Ljungcrantz, L. Hultman, M. Grimsditch, Enhanced mechanical hardness in epitaxial nonisostructural Mo/NbN and W/NbN superlattices, J. Appl. Phys. 84 (1998) 776–785.
[33] A. Kamlapure, M. Mondal, M. Chand, A. Mishra, J. Jesudasan, V. Bagwe, L. Benfatto, V. Tripathi, P. Raychaudhuri, Measurement of magnetic penetration depth and superconducting energy gap in very thin epitaxial NbN films, Appl. Phys. Lett. 96 (2010) 072509.
[34] S. Chockalingam, M. Chand, J. Jesudasan, V. Tripathi, P. Raychaudhuri, Superconducting properties and Hall effect of epitaxial NbN thin films, Phys. Rev. B 77 (2008) 214503.
[35] L. Kang, B.B. Jin, X.Y. Liu, X.Q. Jia, J. Chen, Z.M. Ji, W.W. Xu, P.H. Wu, S.B. Mi, A. Pimenov, Y.J. Wu, B.G. Wang, Suppression of superconductivity in epitaxial NbN ultrathin films, J. Appl. Phys. 109 (2011) 033908.
[36] T. Yamashita, K. Hamasaki, T. Komata, Performance of the IFSMTF helium refrigerator in partial-array tests, Adv. Cryog. Eng. Mater. 32 (1986) 617–626.
[37] S.P. Chockalingam, M. Chand, J. Jesudasan, V. Tripathi, P. Raychaudhuri, Evolution of superconducting properties with disorder in epitaxial NbN films, J. Phys. Conf. Ser. 150 (2009) 052035.
[38] Z. Wang, H. Terai, W. Qiu, K. Makise, Y. Uzawa, K. Kimoto, Y. Nakamura, High-quality epitaxial NbN/AlN/NbN tunnel junctions with a wide range of current density, Appl. Phys. Lett. 102 (2013) 142604.
[39] L. Longobardi, D. Massarotti, G. Rotoli, D. Stornaiuolo, G. Papari, A. Kawakami, G.P. Pepe, A. Barone, F. Tafuri, Quantum crossover in moderately damped epitaxial NbN/MgO/NbN junctions with low critical current density, Appl. Phys. Lett. 99 (2011) 062510.
[40] S. Ezaki, K. Makise, B. Shinozaki, T. Odo, T. Asano, H. Terai, T. Yamashita, S. Miki, Z. Wang, Localization and interaction effects in ultrathin epitaxial NbN superconducting films, J. Phys. Condens. Matter 24 (2012) 475702.
[41] J.-C. Villegier, S. Bouat, P. Cavalier, R. Setzu, R.E. de Lamaestre, C. Jorel, P. Odier, B. Guillet, L. Mechin, M.P. Chauvat, P. Ruterana, Epitaxial growth of sputtered ultrathin NbN layers and junctions on sapphire, IEEE Trans. Appl. Supercond. 19 (2009) 3375–3378.
[42] Z. Wang, A. Kawakami, Y. Uzawa, B. Komiyama, Superconducting properties and crystal structures of single-crystal niobium nitride thin films deposited at ambient substrate temperature, J. Appl. Phys. 79 (1996) 7837–7842.
[43] R.E. Treece, M.S. Osofsky, E.F. Skelton, S.B. Qadri, J.S. Horwitz, D.B. Chrisey, New phase of superconducting NbN stabilized by heteroepitaxial film growth, Phys. Rev. B 51 (1995) 9356–9359.
[44] K. Senapati, N.K. Pandey, R. Nagar, R.C. Budhani, Normal-state transport and vortex dynamics in thin films of two structural polymorphs of superconducting NbN, Phys. Rev. B 74 (2006) 104514.
[45] T. Shapoval, H. Stopfel, S. Haindl, J. Engelmann, D.S. Inosov, B. Holzapfel, V. Neu, L. Schultz, Quantitative assessment of pinning forces and magnetic penetration depth in NbN thin films from complementary magnetic force microscopy and transport measurements, Phys. Rev. B 83 (2011) 214517.
[46] M. Kidszun, R. Hühne, B. Holzapfel, L. Schultz, Ion-beam-assisted deposition of textured NbN thin films, Supercond. Sci. Technol. 23 (2010) 025010.
[47] R.E. Treece, J.S. Horwitz, S.B. Qadri, E.F. Skelton, E.P. Donovan, D.B. Chrisey, Metastable nitride synthesis by pulsed laser deposition: a new phase in the NbNx system, J. Solid State Chem. 117 (1995) 294–299.
[48] C.P. Mulligan, D. Gall, CrN-Ag self-lubricating hard coatings, Surf. Coat. Technol. 200 (2005) 1495–1500.
[49] J.M. Purswani, T. Spila, D. Gall, Growth of epitaxial Cu on MgO(001) by magnetron sputter deposition, Thin Solid Films 515 (2006) 1166–1170.
[50] R. Deng, S.R. Evans, D. Gall, Bandgap in $Al_{1-x}Sc_xN$, Appl. Phys. Lett. 102 (2013) 112103.
[51] J.R. Frederick, J. D'Arcy-Gall, D. Gall, Growth of epitaxial CrN on MgO(001): role of deposition angle on surface morphological evolution, Thin Solid Films 494 (2006) 330–335.
[52] F. Tian, J. D'Arcy-Gall, T.Y. Lee, M. Sardela, D. Gall, I. Petrov, J.E. Greene, Epitaxial $Ti_{1-x}W_xN$ alloys grown on MgO(001) by ultrahigh vacuum reactive magnetron sputtering: electronic properties and long-range cation ordering, J. Vac. Sci. Technol. A 21 (2003) 140–146.
[53] S. Kodambaka, V. Petrova, S.V. Khare, D. Gall, A. Rockett, I. Petrov, J.E. Greene, Size-dependent detachment-limited decay kinetics of two-dimensional TiN islands on TiN(111), Phys. Rev. Lett. 89 (2002) 176102.
[54] X.Y. Zhang, D. Gall, CrN electronic structure and vibrational modes: an optical analysis, Phys. Rev. B 82 (2010) 045116.
[55] M.A. Wall, D.G. Cahill, I. Petrov, D. Gall, J.E. Greene, Nucleation kinetics during homoepitaxial growth of TiN(001) by reactive magnetron sputtering, Phys. Rev. B 70 (2004) 035413.
[56] C.S. Shin, D. Gall, P. Desjardins, A. Vailionis, H. Kim, I. Petrov, J.E. Greene, M. Oden, Growth and physical properties of epitaxial metastable cubic TaN(001), Appl. Phys. Lett. 75 (1999) 3808–3810.
[57] J.R. Frederick, D. Gall, Surface morphological evolution of epitaxial CrN(001) layers, J. Appl. Phys. 98 (2005) 054906.
[58] J.S. Chawla, X.Y. Zhang, D. Gall, Effective electron mean free path in TiN(001), J. Appl. Phys. 113 (2013) 063704.
[59] X.Y. Zhang, D. Gall, Surface mound formation during epitaxial growth of CrN(001), Thin Solid Films 518 (2010) 3813–3818.
[60] R. Deng, B.D. Ozsdolay, P.Y. Zheng, S.V. Khare, D. Gall, Optical and transport measurement and first-principles determination of the ScN band gap, Phys. Rev. B 91 (2015) 045104.
[61] D. Gall, M. Stoehr, J.E. Greene, Vibrational modes in epitaxial $Ti_{1-x}Sc_xN$(001) layers: an ab initio calculation and raman spectroscopy study, Phys. Rev. B 64 (2001) 174302.

[62] W.C. Oliver, G.M. Pharr, An improved technique for determining hardness and elastic moculus using load and displacement sensing indentation experiments, J. Mater. Res. 7 (1992) 1564.
[63] J.P. Perdew, K. Burke, M. Ernzerhof, Generalized gradient approximation made simple, Phys. Rev. Lett. 77 (1996) 3865.
[64] G. Kresse, D. Joubert, From ultrasoft pseudopotentials to the projector augmented-wave method, Phys. Rev. B 59 (1999) 1758.
[65] V.I. Ivashchenko, P.E.A. Turchi, E.I. Olifan, Phase stability and mechanical properties of niobium nitrides, Phys. Rev. B 82 (2010) 054109.
[66] J. Paier, M. Marsman, K. Hummer, G. Kresse, I.C. Gerber, J.G. Ángyán, Screened hybrid density functionals applied to solids, J. Chem. Phys. 124 (2006) 154709.
[67] L. Hultman, S.A. Barnett, J.E. Sundgren, J.E. Greene, Growth of epitaxial TiN films deposited on MgO(100) by reactive magnetron sputtering: the role of low-energy ion irradiation during deposition, J. Cryst. Growth 92 (1988) 639–656.
[68] J.B. Hudson, Thermodynamics of Materials, John Wiley and Sons, 1996.
[69] M. Denis, W.G. Richard, B. Pascal, H. Marcus, P. Daniel, Vacancy filling effect in thermoelectric NbO, J. Phys. Condens. Matter 27 (2015) 115501.
[70] W.E. Pickett, E.C. Ethridge, S.C. Erwin, Niobium nitride: stability and integrity of the "NbO phase", Solid State Commun. 100 (1996) 691–693.
[71] M.J. Mehl, D. Finkenstadt, C. Dane, G.L.W. Hart, S. Curtarolo, Finding the stable structures of WN with an ab initio high-throughput approach, Phys. Rev. B 91 (2015) 184110.
[72] R. Hill, The elastic behaviour of a crystalline aggregate, Proc. Phys. Soc. London, Sect. A 65 (1952) 349–355.
[73] J.J. Vlassak, W.D. Nix, Measuring the elastic properties of anisotropic materials by means of indentation experiments, J. Mech. Phys. Solids 42 (1994) 1223–1245.
[74] J.J. Vlassak, W.D. Nix, Indentation modulus of elastically anisotropic half spaces, Philos. Mag. A 67 (1993) 1045–1056.
[75] J.M.J.d. Toonder, J.A.W.v. Dommelen, F. Baaijens, The relation between single crystal elasticity and the effective elastic behaviour of polycrystalline materials: theory, measurement and computation, Model. Simul. Mater. Sci. Eng. 7 (1999) 909–928.
[76] J.-E. Sundgren, B.O. Jahansson, A. Rockett, S.A. Barnett, J.E. Greene, Physics and chemistry of protective coatings, Am. Inst. Phys. Conf. Proc. 149 (1986) 95–115.
[77] C.S. Shin, Y.W. Kim, D. Gall, J.E. Greene, I. Petrov, Phase composition and microstructure of polycrystalline and epitaxial TaNx layers grown on oxidized Si(001) and MgO(001) by reactive magnetron sputter deposition, Thin Solid Films 402 (2002) 172–182.
[78] D. Gall, S. Kodambaka, M.A. Wall, I. Petrov, J.E. Greene, Pathways of atomistic processes on TiN(001) and (111) surfaces during film growth: an ab initio study, J. Appl. Phys. 93 (2003) 9086–9094.
[79] M.A. Wall, D.G. Cahill, I. Petrov, D. Gall, J.E. Greene, Nucleation kinetics versus nitrogen partial pressure during homoepitaxial growth of stoichiometric TiN(001): a scanning tunneling microscopy study, Surf. Sci. 581 (2005) L122–L127.
[80] P.v.d. Sluis, Determination of strain in epitaxial semiconductor layers by high-resolution X-ray diffraction, J. Phys. D. Appl. Phys. 26 (1993) A188.
[81] D. Gall, I. Petrov, P. Desjardins, J.E. Greene, Microstructural evolution and Poisson ratio of epitaxial ScN grown on TiN(001)/MgO(001) by ultrahigh vacuum reactive magnetron sputter deposition, J. Appl. Phys. 86 (1999) 5524–5529.
[82] J.O. Kim, J.D. Aschenbach, P.B. Mirkarimi, M. Shinn, S.A. Barnett, Elastic constants of single crystal transition metal nitride films measured by line focus acoustic microscopy, J. Appl. Phys. 72 (1992) 1805.
[83] P. Kroll, Hafnium nitride with thorium phosphide structure: physical properties and an assessment of the Hf–N, Zr–N, and Ti–N phase diagrams at high pressures and temperatures, Phys. Rev. Lett. 90 (2003) 125501.
[84] U. Wiklund, M. Bromark, M. Larsson, P. Hedenqvist, S. Hogmark, Cracking resistance of thin hard coatings estimated by four-point bending, Surf. Coat. Technol. 91 (1997) 57–63.
[85] G.i. Oya, Y. Onodera, Transition temperature and crystal structure of single-crystal and polycrystalline NbNx films, J. Appl. Phys. 45 (1974) 1389.
[86] H. Ljungcrantz, M. Odén, L. Hultman, J.E. Greene, J.-E. Sundgren, Nanoindentation studies of single crystal (001), (011), and (111) oriented TiN layers on MgO, J. Appl. Phys. 80 (1996) 6725.
[87] C.S. Shin, D. Gall, N. Hellgren, J. Patscheider, I. Petrov, J.E. Greene, Vacancy hardening in single-crystal TiNx(001) layers, J. Appl. Phys. 93 (2003) 6025–6028.
[88] H. Kindlund, D.G. Sangiovanni, J. Lu, J. Jensen, V. Chirita, J. Birch, I. Petrov, J.E. Greene, L. Hultman, Vacancy-induced toughening in hard single-crystal V0.5Mo0.5Nx/MgO(001) thin films, Acta Mater. 77 (2014) 394–400.
[89] X.Y. Zhang, J.S. Chawla, R.P. Deng, D. Gall, Epitaxial suppression of the metal–insulator transition in CrN, Phys. Rev. B 84 (2011) 073101.
[90] X.Y. Zhang, J.S. Chawla, B.M. Howe, D. Gall, Variable-range hopping conduction in epitaxial CrN(001), Phys. Rev. B 83 (2011) 165205.
[91] D. Gall, I. Petrov, J.E. Greene, Epitaxial Sc1-xTixN(001): optical and electronic transport properties, J. Appl. Phys. 89 (2001) 401–409.
[92] R. Deng, P.Y. Zheng, D. Gall, Optical and electron transport properties of rock-salt Sc1–xAlxN, J. Appl. Phys. 118 (2015) 015706.
[93] K. Zhang, K. Balasubramanian, B.D. Ozsdolay, C.P. Mulligan, S.V. Khare, W.T. Zheng, D. Gall, Epitaxial NbCxN1–x(001) layers: growth, mechanical properties, and electrical resistivity, Surf. Coat. Technol. 277 (2015) 136–143.